Absence of Dipeptidyl Peptidase 3 Increases Oxidative Stress and Causes Bone Loss

Ciro Menale[1,2], **Lisa J Robinson**[3], **Eleonora Palagano**[1,2], **Rosita Rigoni**[1,2], **Marco Erreni**[4], **Alejandro J Almarza**[5], **Dario Strina**[1,2], **Stefano Mantero**[1,2], **Michela Lizier**[1,2], **Antonella Forlino**[6], **Roberta Besio**[6], **Marta Monari**[7], **Paolo Vezzoni**[1,2], **Barbara Cassani**[1,2], **Harry C Blair**[8], **Anna Villa**[1,2], **Cristina Sobacchi**[1,2]

[1]Consiglio Nazionale delle Ricerche–Istituto di Ricerca Genetica e Biomedica (CNR-IRGB), Milan Unit, Milan, Italy

[2]Humanitas Clinical and Research Center–Istituto di Ricovero e Cura a Carattere Scientifico (IRCCS), Rozzano, Italy

[3]Department of Pathology, West Virginia University, Morgantown, WV, USA

[4]Unit of Advanced Optical Microscopy, Humanitas Clinical and Research Center–Istituto di Ricovero e Cura a Carattere Scientifico (IRCCS), Rozzano, Italy

[5]Department of Oral Biology, Department of Bioengineering, McGowan Institute of Regenerative Medicine, University of Pittsburgh, Pittsburgh, PA, USA

[6]Department of Molecular Medicine, Unit of Biochemistry, University of Pavia, Pavia, Italy

[7]Clinical Investigation Laboratory, Humanitas Clinical and Research Center–Istituto di Ricovero e Cura a Carattere Scientifico (IRCCS), Rozzano, Italy

[8]Veterans' Affairs Medical Center and Department of Pathology, University of Pittsburgh, Pittsburgh, PA, USA

Abstract

Controlling oxidative stress through the activation of antioxidant pathways is crucial in bone homeostasis, and impairments of the cellular defense systems involved contribute to the pathogenesis of common skeletal diseases. In this work we focused on the dipeptidyl peptidase 3 (DPP3), a poorly investigated ubiquitous zinc-dependent exopeptidase activating the Keap1-Nrf2 antioxidant pathway. We showed *Dpp3* expression in bone and, to understand its role in this compartment, we generated a *Dpp3* knockout (KO) mouse model and specifically investigated the skeletal phenotype. Adult *Dpp3* KO mice showed a mild growth defect, a significant increase in bone marrow cellularity, and bone loss mainly caused by increased osteoclast activity. Overall, in the mouse model, lack of DPP3 resulted in sustained oxidative stress and in alterations of bone microenvironment favoring the osteoclast compared to the osteoblast lineage. Accordingly, in vitro

Disclosures

All authors state that they have no conflicts of interest.

Additional Supporting Information may be found in the online version of this article.

studies revealed that *Dpp3* KO osteoclasts had an inherent increased resorptive activity and ROS production, which on the other hand made them prone to apoptosis. Moreover, absence of DPP3 augmented bone loss after estrogen withdrawal in female mice, further supporting its relevance in the framework of bone pathophysiology. Overall, we show a nonredundant role for DPP3 in the maintenance of bone homeostasis and propose that DPP3 might represent a possible new osteoimmunological player and a marker of human bone loss pathology.

Keywords

BONE LOSS; DPP3; OSTEOPOROSIS; OXIDATIVE STRESS

Introduction

Bone homeostasis relies on the balance between different skeletal cell functions and on the intricate network of interactions they establish with nonskeletal cells in the bone tissue and in distant organs.[1,2] Alterations of the crosstalk between all these cell types may result in skeletal disorders that often affect bone density, composition, and microarchitecture.[3] Bone mineral density (BMD) is a complex quantitative trait determined by a polygenic component and environmental elements.[4] Among these, oxidative stress has been indicated as an important factor contributing to BMD.[5] In particular, oxidative stress and the elicited molecular and cellular mechanisms have been recognized as crucial players in the pathogenesis of osteoporosis and bone loss diseases, as well as in age-related bone loss.[6]

Oxidative stress refers to the excess of reactive oxygen species (ROS) owing to the imbalance between ROS production and antioxidant responses. In every cell type, ROS are produced by mitochondrial oxidative respiration and by many metabolic processes as intermediates.[7] Their levels are raised by various stimuli, such as hormones, cytokines, hypoxic conditions, or exposure to ionizing radiation, ultraviolet light, or ozone. Moreover, immune cells produce ROS in the framework of defense mechanisms against invading pathogens.[8] Besides playing a role in intracellular functions, ROS are endowed with a highly damaging potential; therefore, cells possess different means for detoxification. In particular, the kelch-like Enoyl coenzyme A (CoA) hydratase (ECH)-associated protein 1 (Keap1)/nuclear factor E2-related factor 2 (Nrf2) antioxidant pathway is a common protective mechanism acting in basal conditions as well as upon induction by oxidative stressors.[9] Nrf2 is a transcription factor regulating the expression of genes coding for antioxidant and detoxifying enzymes, such as heme oxygenase 1 (HO-1), superoxide dismutase (SOD), catalase, glutathione peroxidase (GPX), peroxiredoxin-1 (PRX-1), and NADPH:quinone oxidoreductase 1 (NQO1).[10] In basal conditions, Nrf2 is mainly inactive in the cytoplasm, bound by Keap1 homodimers and targeted to ubiquitin-dependent proteasomal degradation. In response to oxidative stress, Keap1-interactors displace Nrf2, which then migrates into the nucleus and binds the antioxidant response element (ARE) in the promoter of its target genes, as a heterodimer with small Maf proteins.[10] Another transcription factor (BTB and CNC homology 1, Bach1) is involved in transcriptional regulation as a Nrf2 competitor and is shuttled in and out of the nucleus to respectively attenuate or liberate Nrf2 activity in response to different stimuli.[11,12] Reduced Nrf2

activity has been linked to a number of pathological conditions.[13–18] Furthermore, alterations of the Keap1/Nrf2 pathway have been reported in animal models of bone disease, and lack of Nrf2 exacerbated pathological phenotypes.[19–22] In fact, unresolved oxidative stress stimulates osteoclast (OC) formation and osteocyte apoptosis, and affects osteoblast (OB) functions.[5]

In this context, the dipeptidyl peptidase 3 (DPP3) has been recently identified as an upstream activator of the Keap1/Nrf2 antioxidant signaling cascade by binding to Keap1 and favoring Nrf2 function.[23] DPP3 is a ubiquitous cytosolic zinc-exopeptidase, belonging to a large family of metal-dependent peptidases with specific prolyl peptidase activity toward different substrates.[24] It has been purified from several murine and human biological sources and has been proposed to act in the terminal stages of protein turnover, in the framework of several pathophysiological processes through the hydrolysis of bioactive peptides,[24–27] in metabolic, cardiovascular, and neoplastic diseases.[25,26,28–30] For the first time, here we demonstrate DPP3 protein expression in the bone tissue and uncover its role in bone pathophysiology, taking advantage of our newly generated *Dpp3* knockout (KO) mouse model.

Materials and Methods

Animals

All the procedures involving mice were performed in accordance with ethical rules of the Institutional Animal Care and Use Committee of Humanitas Clinical and Research Center and with international laws (Italian Ministry of Health, protocol n.07/2014-PR). Animals were group-housed in a specific-pathogen-free animal facility, under a 12-hour dark/light cycle, with water and food provided *ad libitum*. We used the *Cre/lox* technology to generate mice in which *Dpp3* was ubiquitously inactivated (*Dpp3* KO) through a conventional strategy of blastocyst injection with commercially available, murine embryonic stem cell clones carrying a floxed *Dpp3* allele. All details are available in the Supporting Materials and Methods in File S1.

DPP3 enzymatic activity assay

Total protein extracts were prepared from tail biopsies minced in 150 μL Tris–HCl, pH 7.8, and subjected to sonication and freeze-thawing cycles. For protein extracts from total bone, the tissue was frozen in liquid nitrogen and homogenized using aluminum beads and the TissueLyser II instrument (Qiagen, Hilden, Germany). Tissue debris were removed by centrifugation at 4°C. Protein concentration in the supernatants were estimated using the DC™ Protein Assay Kit II (Bio-Rad, Berkeley, CA, USA) following the manufacturer's instructions, on a Synergy™ H4 Microplate Reader (BioTek Instruments, Inc., Winooski, VT, USA). DPP3 enzymatic activity was performed as reported,[31] with minor modifications. Briefly, 50 to 80 μg of protein extracts were assayed with 0.04 mM Arg-Arg-β-naphthylamide (Sigma-Aldrich, Saint Louis, MO, USA) in 250 μL Tris–HCl, pH 8.5, at room temperature (RT). The reaction was stopped by adding 50 μL of 2 M acetate buffer, pH 4.5, containing 10% Tween and 1.5 mg/mL Fast Blue B Salt (all chemicals from Sigma-Aldrich). The absorbance of the released product (β-naphthylamine) was measured at 530

nm, using Synergy™ H4 Microplate Reader. The enzymatic activity was expressed as percentage of the wild-type (WT) value.

Western blot protein analysis

Total bone protein extracts, gel electrophoresis, transfer, and visualization were performed using standard Western blotting techniques. Briefly, long bones were frozen in liquid nitrogen and homogenized in homemade radioimmunoprecipitation assay (RIPA) buffer supplemented with protease inhibitor (Sigma-Aldrich). Protein concentrations were assessed using DC Protein Assay Kit II (Bio-Rad). Thirty micrograms (30 μg) of protein extracts were separated on a 12% SDS-PAGE, transferred to a nitrocellulose membrane, and probed with an antibody for DPP3 (C-term; Abcam, Cambridge, UK) diluted 1:1000 in 5% milk in 20 mM Tris-buffered saline, pH 7.6, 0.1% Tween 20 (TBST), and with an antibody for β-actin (Sigma-Aldrich) diluted 1:400 in 5% milk in TBST, washed, and probed with a secondary antibody conjugated with horseradish peroxidase (HRP) and developed using the Immobilon™ Western kit (Millipore, Watford, UK). Images were captured using the ChemiDoc™ MP Imaging System equipped with Image Lab™ Software (Bio-Rad).

Histology and immunohistochemistry

Mice were euthanized by CO_2 asphyxiation; tissues were harvested and either fixed in 4% paraformaldehyde (PFA) or processed to obtain cell suspensions for further analysis. Selected bones were decalcified in an Ion Exchange Decal Unit (Biocare Medical, Concord, CA, USA), dehydrated, and embedded in paraffin for hematoxylin and eosin (H&E) staining. For immunohistochemical staining, 3-μm-thick longitudinal serial sections were collected on glass slides, deparaffinized, and treated for antigen retrieval. Tissue sections were incubated with 2% H_2O_2 for 15 minutes in the dark, washed with water, and blocked with Rodent Block M (Biocare Medical, Pacheco, CA, USA) for 40 minutes at RT. Then, they were incubated overnight at 4°C or 1 hour at RT with the following primary antibodies, diluted in PBS 0.05% Tween 20 (PBST) (GIBCO, Grand Island, NY, USA, and Merck Millipore, Burlington, MA, USA, respectively): anti-DPP3, 1:100 (Sigma-Aldrich); anti-Nrf2, 1:100 (Proteintech, Rosemont, IL, USA); anti-HO-1, 1:500 (Bio-Rad); anti-4-Hydroxynonenal, 1:1000 (Abcam, Cambridge, UK). Sections were then rinsed in PBST and incubated with Mach 1 Polymer (Biocare Medical) for 30 minutes at RT, rinsed in PBST, developed with 3,3′-Diaminobenzidine (DAB), and counterstained with hematoxylin. Images were acquired by an Olympus BX51 Microscope and with a VS120 DOT SLIDE BX61 VS instrument (Olympus Optical Co., Ltd, Shinjuku, Tokyo, Japan). Staining was quantified using ImageJ software (NIH, Bethesda, MD, USA; https://imagej.nih.gov/ij/); at least two vertebrae/sections/animal were analyzed ($n = 10$ mice per genotype) and protein expression was represented as percentage of DAB$^+$ area over total vertebral area.

Histomorphometry

Histomorphometry was performed using ImageJ software; parameters were calculated according to the recommendations of the Histomorphometry Nomenclature Committee of the American Society of Bone and Mineral Research.[32,33]

All the dynamic and static histomorphometric evaluations were performed on 6-month-old *Dpp3* KO and WT male mice. For dynamic histomorphometric analysis of bone formation, on days 5 and 2 before euthanization mice received intraperitoneal (i.p.) injections of calcein (20 mg/kg dose). At necropsy, after removal of viscera, the long bones and the spine were fixed in 4% PFA; nondecalcified specimens were frozen in optimal cutting temperature (OCT) cryoembedding compound and stored at −80°C until sectioning. Frozen samples of lumbar vertebrae were cryosectioned, exploiting the CryoJane® Tape-Transfer system and tungsten blades (Leica Biosystems, Wetzlar, Germany). Mineralized surface and interlabel distance were evaluated by measuring calcein labels in the cancellous bone using the grid intersect method, and interlabel distance using minimum pixel interval at high power, as reported.[34] Bone formation parameters were expressed as bone formation rate (BFR) and mineral surface over bone surface (MS/BS).

For static histomorphometric analysis, mouse bones were fixed in 4% PFA, decalcified in 14% ethylenediaminetetraacetic acid (EDTA), pH 7.4 with acetic acid, then dehydrated and embedded in paraffin. Tissue sections were stained with the tartrate resistant acid phosphatase (TRAP) staining kit (Sigma-Aldrich) and counterstained with hematoxylin. Images were acquired with a VS120 DOT SLIDE BX61 VS instrument (Olympus). OC surface/bone surface (%) was calculated in the trabecular region of lumbar vertebrae below the growth plate, as TRAP stained area over total bone area; at least two vertebrae/section/ animal were analyzed (n 5 mice per genotype).

Von Kossa/Van Gieson and alkaline phosphatase (ALP) staining were performed on plastic-embedded spine, according to standard procedures and using a dedicated kit (Sigma-Aldrich). Osteoid thickness was measured in high-power photographs of stained sections, with osteoid thickness corrected for section obliqueness. OB surface/bone surface (%) was calculated in the trabecular region of lumbar vertebrae below the growth plate, as ALP stained area over total bone area; two vertebrae/section/animal were analyzed ($n = 3$ mice per genotype).

All the measurements were performed by a blinded operator.

Micro–computed tomography

Micro–computed tomography (µCT) was performed using a Skyscan 1272 instrument (Bruker, Kontich, Belgium) at 6-µm resolution with 0.25-mm aluminum filter, source voltage 60 kV and current 166 µA. Images were reconstructed using the NRecon and InstaRecon software (Bruker). Cross-sectional images were obtained using Dataviewer software and three-dimensional images using the CTvox software (Bruker). Quantitative histomorphometric analysis of lumbar vertebrae and femoral bone were performed using the Bruker CTan software.

Three-point-bending test

Three-point bending was performed using an Instron 5564 instrument (Instron, Norwood, MA, USA). The bones were positioned horizontally, anterior upward, between 10 mm supports. Load was applied at 500 µm/minutes at mid-diaphysis until failure, with load/ deflection used to calculate stiffness and failure strength.[35]

Fluorescence-activated cell sorting analysis

Cell suspensions from WT and *Dpp3* KO bone marrow (BM) were obtained by flushing long bones from a single hind limb (one femur and one tibia) of each mouse with PBS/2% FBS/5 mM EDTA, and then stained with the following specific fluorescent-conjugated antibodies: CD11b (clone M1/70), Ly-6G (clone 1A8), and F4/80 (clone BM8), to identify polymorphonuclear cells (PMNs) and macrophages, respectively. OC precursor-like cells (OCPs) were identified as $CD3^-B220^-CD11b^{low/-}CD115^+CD117^{hi}$ as reported,[36] by using CD11b (clone M1/70), CD3 (clone 145–2C11), B220 (clone RA3–6B2), CD115 (clone AFS98), and CD117 (clone 2B8).

Antibodies were purchased from either BD Biosciences, Franklin Lakes, NJ, USA, or eBioscience, Inc., San Diego, CA, USA.

All samples were acquired on a BD FACSCanto II flow cytometer (BD Biosciences, Eysins, Switzerland) and analyzed with FlowJo software (Tree Star, Inc., Ashland, OR, USA).

Cytokine ELISA

BM samples were collected by flushing a single hind limb per mouse as above ("Fluorescence-activated cell sorting analysis" paragraph) and spinning at 500g for 5 minutes to remove BM cells. Supernatants were stored at −20°C until use. For ELISA measurements, samples were assayed as such using specific Duo Set ELISA kits for mouse interleukin 1β (IL-1β), tumor necrosis factor α (TNFα), interferon gamma (IFNγ), M-CSF, and IL-10 (R&D Systems, Minneapolis, MN, USA), according to the manufacturer's instructions. Cytokine concentration was normalized to total suspension volume.

For serological measurements, blood was collected without anticoagulants following standard procedures and serum was separated after a few hours by low-speed centrifugation. Samples were stored at −20°C until use. Total calcium and phosphorus levels were determined using a Ci16200 Architect Abbott instrument (Abbott Park, IL, USA). Other parameters were measured using dedicated ELISA kits, such as CTX (CUSABIO, Hubei, China); TRAP (Immunodiagnostic Systems, Ltd., Scottsdale, AZ, USA); RANKL and OPG (Quantikine® kits; R&D Systems); PTH and osteocalcin (Immutopics, Inc., San Clemente, CA, USA); and P1NP (MyBioSource, San Diego, CA, USA). Plate reading was done on a VERSAmax™ Tunable Microplate Reader using the SoftMax Pro 5.3 Data acquisition and Analysis Software.

In vitro OC differentiation and resorption assay

In vitro osteoclastogenesis was induced following standard protocols, as reported.[37] Briefly, 4×10^5 splenocytes/well were cultured in 96-well plates in α-MEM medium (Sigma-Aldrich) supplemented with 10% FBS, 1% penicillin/streptomycin (P/S), and 1% glutamine in the presence of 25 ng/mL murine M-CSF, 5 ng/mL human TGFβ1 (both from Peprotech, London, UK), 1 μM dexamethasone (Sigma-Aldrich), and with or without 100 ng/mL RANKL for 6 days. Mature OCs were stained using the TRAP Kit (Sigma-Aldrich) following the manufacturer's instructions; differentiated TRAP+, multinucleated (nuclei

number 3) OCs were counted by a blind operator and expressed as number of mature OCs per well.

The same culture conditions were applied to osteoclastogenesis on dentin discs (Immunodiagnostic Systems, Ltd., Scottsdale, AZ, USA), in order to evaluate OC resorptive activity. After 3 weeks, dentin discs were rinsed with water, scraped to remove attached cells, stained with 1% Toluidine blue solution for 3 minutes, and then washed with water to visualize resorption pits. Images were acquired on an EVOS XL Inverted Microscope (Thermo Fisher Scientific, Waltham, MA, USA) for both TRAP⁺ mature OCs and Toluidine blue–stained dentin discs. Resorbed dentin area was analyzed by using ImageJ software and expressed as percentage of Toluidine blue–stained area over total dentin area.

Gene expression analysis

Total RNA was extracted from whole tissues, cell suspensions, or cell cultures using the PureZOL™ Reagent (Bio-Rad), following the manufacturer's instructions. Reverse transcription was carried out using 0.5 to 1.0 µg total RNA and High Capacity cDNA Reverse Transcription Kit (Applied Biosystems, Foster City, CA, USA). RT-PCR was performed using primers reported in Supporting Table 1 in File S1. qPCR was performed using SsoAdvanced™ SYBR® Green Supermix (Bio-Rad) and gene-specific primers as detailed in Supporting Table 1 in File S1. The amplification was performed using the ViiA7 Real-Time PCR Detection System (Applied Biosystems) with the following cycling conditions: cDNA denaturation and polymerase activation step at 95°C for 20 seconds followed by 40 cycles of denaturation at 95°C for 1 seconds and annealing at 60°C for 20 seconds; extension step for 60 cycles at 65°C for 30 seconds and melting curve analysis step at 65°C to 95°C with 0.5°C increment for 2 seconds/step. The relative gene expression analysis of target genes was conducted following the comparative $2^{-\Delta Ct}$ method and the normalized expression was calculated as arbitrary units (AU) or fold change mRNA level, as appropriate, in comparison with pertinent controls.

Fluorescence microscopy analysis

For immunofluorescence analysis, OCs were differentiated on glass in the conditions described above in the section "In vitro OC differentiation and resorption assay". Then, cells were fixed in 4% PFA for 10 minutes at RT, permeabilized with 0.5% Triton™ X-100 (Sigma-Aldrich) in PBS and blocked with PBS 5% FBS for 1 hour at RT. The primary antibodies anti-Nrf2, 1:100 (Proteintech) and TRITC-phalloidin, 0.5 µg/mL (Thermo Fisher Scientific) were diluted in blocking buffer and incubated for 30 minutes at RT. The secondary antibody conjugated with Alexa Fluor 488 was incubated for 45 minutes at RT. Nuclei were visualized with DAPI (Thermo Fisher Scientific). Images were acquired with a FluoView FV1000 laser-scanning confocal microscope (Olympus), with 405, 488, and 559 nm wavelength laser excitation for DAPI, Alexa Fluor 488 (Nrf2) and TRITC-phalloidin, respectively. Emission filter bandwidths and sequential scanning acquisition were set up in order to avoid any possible spectral overlap between fluorophores. Images were acquired with a UPLFLN 40× O NA 1.30 objective (Olympus). Fluorescence intensity was quantified in at least six cells per well using ImageJ software.

Second harmonic generation

Second harmonic generation (SHG) was collected with a Trim-scope II two-photon microscope (LaVision BioTec, Bielefeld, Germany). SHG was obtained illuminating samples with a Chameleon Ultra II laser (Coherent, Santa Clara, CA, USA) tuned at 840 nm for two-photon excitation. Measurements were performed on the confocal system previously described with a 20× water immersion objective (XLUMPlanFLn, N.A.1.00; Olympus). Acquisition and instrument control were performed using ImSpector Pro software (LaVision BioTec). At least three random fields per dentin were acquired. 3D reconstruction was performed with Imaris software (Bitplane, Belfast, Ireland); image analysis for resorbed volume quantification was performed using ImageJ software.

ROS production and apoptosis

For the OC lineage, OC precursors were plated in the same medium described in th "In vitro OC differentiation and resorption assay" section (2.5×10^6 cells/well in 24-well plates). Forty-eight hours after induction cells were treated with CellROX® Deep Red Reagent (Thermo Fisher Scientific) for 30 minutes, and analysed by FACS, following the manufacturer's instructions. The same experiment was performed adding lipopolysaccharide (LPS, 0.5 μg/mL), N-AcetylCysteine (NAC, 10 mM), an LPS/NAC combination, or dimethyl fumarate (DMF, 5 μM) to the induction medium for additional 30 minutes (all reagents purchased from Sigma Aldrich).

For PMN cells and macrophages, the BM cell suspension (1×10^6 cells/well in a 96-well plate) was plated in RPMI 1640 medium, 10% FBS, 1% P/S, 1% glutamine, adding CellROX® Deep Red Reagent for 30 minutes, then stained with the following specific fluorescent-conjugated antibodies: CD11b (clone M1/70), Ly-6G (clone 1A8), and F4/80 (clone BM8), and analyzed by FACS.

For PMN cells, the same experiment was performed adding 8 μM phorbol myristate acetate (PMA; Sigma-Aldrich) to the medium for additional 30 minutes, as oxidative stressor.

Apoptotic cells were evaluated by Annexin V/propidium iodide (PI) staining followed by FACS in the same experimental conditions as above. Early apoptotic cells were identified as Annexin V^+PI^-.

OC-OB co-culture

Calvarial OBs were isolated from WT and *Dpp3* KO newborn mice ($n = 3$ per genotype) as described in Supporting Materials and Methods in File S1. Cells were seeded in 48-well plates (2.0×10^4 cells/well) and cultured in α-MEM supplemented with 15% FBS, 1% P/S, and 1% glutamine (OB medium). The day after, 1×10^6 BM cells, obtained by flushing long bones from 6-week-old male WT and *Dpp3* KO mice ($n = 3$ per genotype), were plated on an OB layer and cultured in OB medium supplemented with 10 nM $1,25(OH)_2D_3$ and 1 mM PGE_2 (both from Sigma Aldrich) for 7 days. At the end of the differentiation period, cells were either fixed for the evaluation of TRAP staining and OC counting, or stained for ALP to assess OB activity or processed for RNA isolation and gene expression analysis, as described. The experiments were performed by co-culturing cells as follows: WT OC/WT

OB, KO OC/KO OB, WT OC/KO OB, and KO OC/WT OB. Images were acquired on an EVOS XL Inverted Microscope.

Ovariectomy

Twelve-week-old WT and *Dpp3* KO female mice were anesthetized by i.p. injection of a mixture of 100 mg/kg ketamine and 10 mg/kg xylazine, and subsequently subjected to surgical ovariectomy (OVX) or sham operation (SHAM), according to standard procedures. After surgery, the mice were gently warmed and returned to their cages when they had recovered. All animals were weighed prior to surgery and at necropsy, 6 weeks later; increased body weight in OVX mice as compared to SHAM was considered an indicator of effective estrogen deprivation, as commonly accepted. At euthanasia, uteri were weighed to confirm estrogen suppression in OVX as compared to SHAM mice. Bones were processed for further investigations as reported in the "Histology and immunohistochemistry" and "Micro-computed tomography" sections.

Statistics

Statistical analysis was performed using Mann–Whitney test or *t* test when comparing two groups. One-way or two-way ANOVA with Tukey's post-test were used for multiple comparisons (GraphPad Prism 5.0; GraphPad Software, Inc., La Jolla, CA, USA). Statistical significance was considered when $p < .05$ (*$p < .05$, **$p < .01$, ***$p < .001$). All the experiments were performed at least in triplicate. All data are presented as mean ± SE, unless otherwise stated.

Results

DPP3 is expressed in the bone tissue

To assess DPP3 expression in the bone tissue, we performed immunohistochemical analysis on murine WT bone with a specific anti-DPP3 antibody, and detected protein expression in skeletal cells, such as chondrocytes and cells of the OB lineage also including osteocytes (Fig. 1A). Cells of the myeloid lineage were positively stained, too (Fig. 1A), in line with data in literature describing DPP3 in many different cells of hematopoietic origin.[24] Moreover, we evaluated murine *Dpp3* expression in in vitro differentiated OCs and OC precursors in the absence of RANKL stimulus, and in bone marrow-derived mesenchymal stromal cells (BM-MSCs) and in vitro differentiated OBs. We confirmed *Dpp3* was expressed in all these cell types (Fig. 1B). Based on this evidence and on data from literature, we reasoned it might be relevant to ascertain the potential involvement of DPP3 in bone metabolism.

Absence of DPP3 leads to a bone loss phenotype in mouse

We generated a murine model with constitutive inactivation of the *Dpp3* gene. *Dpp3* KO mice were born from heterozygous breeding pairs at the expected Mendelian ratio. Semiquantitative RT-PCR on several tissues confirmed lack of *Dpp3* gene expression in *Dpp3* KO samples (Fig. 2A). Accordingly, qPCR analysis on total bone and splenocytes showed absent *Dpp3* expression (Fig. 2B), and evaluation of DPP3 enzymatic activity in protein extracts from tail biopsies and total bone demonstrated lack of peptidase activity in

the KO (Fig. 2C). Moreover, Western blot analysis confirmed the absence of the DPP3 protein in *Dpp3* KO total bone (Fig. 2D).

Dpp3 KO mice were fertile, had a normal life span, and were not clearly distinguishable from WT; in fact, μCT analysis of the lumbar spine did not show any difference between WT and KO at 2 months of age (Supporting Fig. 1 in File S1). Interestingly, at an older age (6 months) *Dpp3* KO mice showed a significant reduction in body weight and length, a tendency to reduced long-bone length, and a significant increase in BM cellularity as compared to WT (Fig. 3A). μCT analysis of the lumbar spine showed in *Dpp3* KO mice a significant reduction of bone volume over total volume ratio (BV/TV) and trabecular thickness (Tb.Th), and a significant increase in bone surface over bone volume ratio (BS/BV) and trabecular spacing (Tb.Sp) (Fig. 3B). Accordingly, histochemical evaluation of TRAP-positive cells in bone showed a marked increase of OC surface over bone surface (Oc.S/BS) in the *Dpp3* KO mice (Fig. 3C); in parallel, OB surface over bone surface (Ob.S/BS), assessed by ALP staining, was slightly reduced in *Dpp3* KO mice as compared to WT (Fig. 3D). Dynamic histomorphometry after calcein double labeling of bone revealed a significant reduction in the bone formation rate (BFR) and in the mineralized surface over bone surface ratio (MS/BS) (Fig. 3E), and von Kossa staining of undecalcified bone showed increased osteoid thickness and area in *Dpp3* KO mice as compared to the WT (Fig. 3F), suggesting decreased incorporation of mineral into the matrix by *Dpp3* KO OBs.

μCT analysis of the femur found a trend toward increased cortical porosity in the *Dpp3* KO mice, with no difference in all the other evaluated cortical parameters (Supporting Fig. 2a in File S1). Three-point bending test of cortical bone mechanical properties showed a tendency toward reduction in the stiffness of bones from *Dpp3* KO mice as compared to WT mice; however, the difference did not reach statistical significance (Supporting Fig. 2b in File S1). Similarly, the deflection and fracture load measured for the tibia and femur did not significantly differ between the two genotypes (Supporting Fig. 2b in File S1).

Finally, qPCR analysis on total bone revealed a significant reduction in osteoprotegerin (*Opg*) and increase in receptor activator of nuclear factor kappa-B ligand (*Rankl*) gene expression in *Dpp3* KO mice (Fig. 4A). On the other hand, serum RANKL/OPG ratio was significantly decreased in *Dpp3* KO mice (Fig. 4B), possibly due to the contribution of other cell types to OPG levels in the circulation.[38,39] Serological analysis revealed also a significant increase in TRAP and carboxyterminal collagen cross-links (CTX) levels in *Dpp3* KO mice, in line with enhanced bone resorption observed in the skeletal tissue, and a tendency to a reduction in parathyroid hormone (PTH), whereas no difference was found in serum total calcium and phosphate, procollagen type 1 N-terminal propeptide (P1NP), and osteocalcin levels (Fig. 4B).

Overall, these data suggested that lack of DPP3 resulted in an alteration of the bone tissue and metabolism leading to a bone loss phenotype, which could be ascribed mainly to increased OC resorptive activity; OB activity seemed to be affected, too, specifically with respect to mineral deposition.

Lack of DPP3 reduces Nrf2 function in bone and increases oxidative stress

Based on DPP3 role in the Keap-1/Nrf2 antioxidant pathway, we assessed whether lack of DPP3 altered this pathway in bone. Immunohistochemical analysis with specific antibodies showed significantly reduced expression of Nrf2 and its downstream target heme oxygenase 1 (HO-1), suggesting a possible impairment of the antioxidant capacity of the tissue (Fig. 5A). ROS accumulation can cause a number of cell injuries, in particular lipid peroxidation and increase in the highly toxic aldehyde product 4-hydroxynonenal (4-HNE), which is recognized as a sensitive marker of oxidative damage.[40] In agreement with evidence of altered antioxidant capacity, immunostaining for 4-HNE highlighted increased lipid peroxidation and, by extension, enhanced oxidative stress in the bone tissue of *Dpp3* KO mice (Fig. 5A).

Next, we investigated ex vivo ROS production by BM cells, in particular phagocytic leukocytes as professional ROS producing cells known to express *Dpp3*.[41,42] FACS analysis showed that PMNs were increased in *Dpp3* KO BM as compared to WT (Fig. 5B), whereas no difference was found in the macrophage population. Of note, in both compartments ROS production was significantly higher in the KO as compared to the WT (Fig. 5B).

Oxidative stress and inflammation have been recognized as partners in crime undermining bone homeostasis[22,43]; thus, we assessed the inflammatory status of *Dpp3* KO bone microenvironment. Gene expression analysis showed a significant upregulation of the expression of the inflammatory pro-osteoclastogenic cytokines IL6, IL1β, and TNFα in *Dpp3* KO BM cells (Fig. 5C), which resulted in an increased amount of IL1β and TNFα in the *Dpp3* KO BM supernatant (Fig. 5D). Moreover, we found increased levels of IFNγ and IL10 (Fig. 5D). Overall, the abundance of proinflammatory cytokines over anti-inflammatory ones, together with enhanced oxidative stress likely resulted in a microenvironment conducive for OC formation. In fact, we found higher numbers of OC precursor cells (identified as CD115$^+$CD117^{hi}, gating on CD3$^-$B220$^-$CD11b$^{lo/-}$ cells)[36] in *Dpp3* KOBM (Fig. 5E) and increased levels of M-CSFin the *Dpp3* KO BM supernatant (Fig. 5F).

Loss of DPP3 increases in vitro OC resorption activity and impairs Nrf2 signaling

ROS act as intracellular signaling molecules during RANKL-dependent OC differentiation, but they may have cytotoxic effects, too. In this framework, the Keap1/Nrf2 axis contributes in the regulation of RANKL-dependent osteoclastogenesis through modulation of intracellular ROS levels via expression of cytoprotective enzymes.[44–46] Based on this and on the evidence from histology and immunohistochemistry analysis, we sought to determine the relevance of DPP3 specifically in the OC lineage. To this end, we conducted in vitro OC formation assays from *Dpp3* KO and WT OC precursors, and found lower numbers of differentiated OCs in the KO as compared to the WT on plastic (Fig. 6A), but no difference in the differentiation kinetics (Supporting Fig. 3a in File S1) and in the kinetics of gene expression (Supporting Fig. 3b in File S1) and in the kinetics of gene expression (Supporting Fig. 3b in File S1), in a time-course experiment. In addition, we performed actin staining after OC differentiation on glass and dentin discs, to visualize podosome belt and actin rings.

In both conditions, we did not highlight major differences between WT and *Dpp3* KO OCs (Supporting Fig. 3c in File S1) and in the kinetics of gene expression (Supporting Fig. 3c in File S1).

We observed a comparable resorbed surface in *Dpp3* KO and WT OC cultures on dentin, by means of Toluidine blue staining and corresponding quantification. Of note, when we measured the pit volume through SHG by two-photon confocal microscopy, we found a clear increase of the volume resorbed by KO cells as compared to the WT (Fig. 6A). Accordingly, qPCR analysis demonstrated increased expression of the cathepsin K (*Ctsk*) and metalloproteinase 9 (*Mmp9*) genes, markers of the resorptive function, in Dpp3 KO versus WT OCs (Fig. 6B).

Moreover, we investigated Nrf2 signaling in mature OCs and found reduced expression of *Nrf2* and *Ho-1* by qPCR analysis, and reduced Nrf2 protein by immunofluorescence on mature OCs differentiated on glass, pointing to an imbalance of this antioxidant pathway in the absence of DPP3, as previously observed in the total bone tissue (Fig. 6B,C). We also assessed the expression of other genes involved either in the regulation of the Nrf2 pathway (Sequestosome 1, *Sqstm1*, and *Bach1*) or in ROS detoxification (*Sod1*), and did not find changes in in vitro differentiated *Dpp3* KO OCs as compared to the WT (Supporting Fig. 3d in File S1). Finally, we measured the expression of *Dpp4*, another member of the dipeptidyl peptidase family recently implicated in bone metabolism,[47,48] and we did not find significant changes either in total bone or in in vitro differentiated OCs (Supporting Fig. 3e in File S1).

Overall, these in vitro data suggested that lack of DPP3 caused increased OC resorptive capacity, in agreement with results in vivo; this was likely related to the alteration of Nrf2 antioxidant pathway. On the contrary, absence of DPP3 did not seem to affect the kinetics of OC formation and maturation.

Loss of DPP3 alters ROS production and cell apoptosis

RANKL stimulation is known to induce transient ROS increase, and they have been involved in the RANKL/RANK signaling as a second messenger.[44–46,49] Therefore, we specifically investigated ROS formation in the OC lineage. We found that, after priming, ROS production increased both in the WT and in the KO, as expected, but importantly the percentage of ROS-producing cells and the amount of ROS generated were higher in *Dpp3* KO OC precursors as compared to the WT (Fig. 7A), possibly due to ROS accumulation caused by reduced antioxidant capacity in the KO. Then, we measured ROS production by *Dpp3* KO and WT precursor cells after osteoclastogenic induction in the presence of either NAC, as a general antioxidant, or LPS, as an oxidative stressor, or a combination of the two. NAC treatment alone did not affect ROS production by WT OC precursor cells (OCPs), whereas it restored normal levels of ROS+ OCPs and ROS production in *Dpp3* KO OCPs. On the other hand, after LPS we observed no change in the percentage of ROS-producing cells both in the WT and in the KO, but strikingly, the amount of ROS production increased in the WT and not in the KO. Finally, stimulation with the combination LPS/NAC abrogated ROS increase in the WT and, more importantly, restored normal ROS levels in the KO (Fig. 7B). Of note, we observed normalization of ROS production in *Dpp3* KO OCPs also after

treatment with dimethyl fumarate (DMF), which is a known agonist of the Nrf2 pathway[50]; in parallel, no change in ROS levels was found in WT OCPs upon DMF treatment (Supporting Fig. 4a in File S1).

We hypothesized that the various stimuli provided might have had an impact on cell viability, which would also explain the reduced number of *Dpp3* KO OCs in vitro. Therefore, we measured cell apoptosis in each condition (i.e., M-CSF/RANKL; M-CSF/RANKL + NAC; M-CSF/RANKL + LPS; and M-CSF/RANKL + LPS/NAC) (Fig. 7C). Of note, in all cases, we observed a higher percentage of early apoptotic cells in *Dpp3* KO cell cultures as compared to the WT. In particular, in basal conditions (i.e., MCSF/RANKL) *Dpp3* KO early apoptotic cells comprised a higher percentage of ROS-producing cells, which however generated the same ROS amount as the WT. NAC alone did not have a significant effect in this context, even though there was a trend toward normalization in *Dpp3* KO OCPs. LPS exposure further increased the percentage of *Dpp3* KO early apoptotic cells and the percentage of ROS$^+$ cells as compared to the KO basal condition and to the LPS-stimulated WT; on the contrary, the amount of ROS produced was similar to their WT counterpart, possibly owing to limited cell viability under persistent oxidative stress. Finally, in the presence of LPS and NAC this increase was abrogated and ROS production restored to the WT range in *Dpp3* KO OCPs (Fig. 7C).

In agreement with these data in the OC lineage, *Dpp3* KO PMN stimulated in vitro with PMA increased ROS production as compared to their basal condition, but did not reach the levels of PMA-stimulated WT cells, possibly because of higher apoptosis (Supporting Fig. 4b in File S1). Indeed, the percentage of early apoptotic cells significantly increased after PMA treatment, and even more markedly in *Dpp3* KO PMN, which resulted in lower ROS production.

Based on this, we assessed apoptosis in the skeletal tissue, by performing TUNEL immunostaining on bone sections of WT and *Dpp3* KO mice. TUNEL-positive cells appeared to be predominantly BM cells and interestingly, at variance with in vitro results, apoptosis was significantly reduced in the KOas compared to the WT (Fig. 7D). We hypothesize that this might be due to activation of phagocytic cells in the BM compartment, which possibly tried to dampen oxidative stress and inflammation by enhancing clearance of apoptotic cells,[51] as well as production of anti-inflammatory cytokines, such as IL10. This latter in turn might inhibit apoptosis[52] and enhance efferocytosis by BM phagocytes and subsequent release of factors that fuel the remodeling process.[53]

Absence of DPP3 affects in vitro OB activity and OC-OB crosstalk

To investigate the OB lineage, we evaluated the osteogenic capacity in *Dpp3* KO colony forming unit–OBs (CFU-OBs) and found that it was mildly increased compared to WT, as shown by Alizarin red staining and gene expression analysis (Supporting Fig. 5a,b in File S1). *Nrf2* gene expression did not change, while *Ho-1* increased and *Sod1* and *Foxo-1* had a trend in the same direction, pointing to the activation of possible compensatory mechanisms[54–56] (Supporting Fig. 5c in File S1).

Time-course analysis of the osteogenic process starting from WT and *Dpp3* KO primary calvarial OBs showed increase of Alizarin red staining overtime in both groups, and a tendency to enhanced osteogenesis in *Dpp3* KO versus WT (Supporting Fig. 5d in File S1). Accordingly, the overall expression of osteogenic marker genes showed a trend toward an increase in *Dpp3* KO as compared to WT OBs (Supporting Fig. 5e in File S1).

Both OB mineralization and apoptosis involve the translocation of phosphatidylserine (PS) from the inner to the outer leaflet of the plasma membrane, which can be revealed by Annexin V staining. FACS analysis of *Dpp3* KO and WT primary OBs in basal medium and after 7 days of osteogenic induction showed that the proportion of Annexin V$^+$ cells increased in both groups upon osteogenic induction as compared to the unstimulated condition. In addition, irrespective of stimulation, PS externalization was comparable in *Dpp3* KO and WT primary OBs (Supporting Fig. 5f in File S1). This indicated that the increased in vitro mineralization by *Dpp3* KO OBs was not associated with augmented PS externalization.

Finally, the analysis of antioxidant gene expression recapitulated the findings obtained from CFU-OBs (Supporting Fig. 5g in File S1).

Next, we performed OB/OC co-culture experiments. We found that, regardless of the accompanying OB genotype, *Dpp3* KO OC precursors generated a higher number of mature OCs as compared to WT ones (Fig. 8A). Moreover, in co-cultures of *Dpp3* KO OCs and *Dpp3* KO OBs we found reduced ALP staining and gene expression as compared to WT co-cultures (Fig. 8B).

These results were in line with in vivo evidence and could suggest that the absence of DPP3 altered the crosstalk between the OC and the OB lineage: on one hand, it increased *Dpp3* KO OC precursors' responsiveness to OB-derived molecular cues; on the other, it reduced OB activity. Therefore, we evaluated the expression of coupling factors, namely RANKL, OPG, *Ephb4*, *Wnt5a*, and *Lrp5* for the OB side, *Bmp6*, *Efnb2*, *Wnt10b*, *Sema4d*, and *Ror2* for the OC side.[2,57] We found that KO OC/KO OB, KO OC/WT OB, and WT OC/WT OB co-cultures produced a similar amount of RANKL, which was higher than that in WT OC/KO OB co-cultures (Fig. 8C); on the contrary, the amount of OPG did not vary in the different conditions (Supporting Fig. 6a in File S1). Bmp6 expression was significantly reduced in the presence of KO OC, while it did not differ between WT OC/WT OB and WT OC/KO OB (Fig. 8D); based on BMP6's role in promoting osteoprogenitor recruitment, proliferation, and bone formation,[58] our result was in accordance with reduced ALP staining in KO OC/KO OB co-cultures. Moreover, Efnb2 expression was significantly reduced in KO OC/KO OB co-cultures as compared to WT OC/WT OB ones (Fig. 8D), whereas no difference was found for its receptor EphB4 (Supporting Fig. 6b in File S1). Efnb2-EphB4 bidirectional signaling is known to reduce OC differentiation and to stimulate bone formation[59]; therefore, their relative balance in our experimental model, together with all other data provided so far, supported skewing of bone metabolism in favor of bone resorption rather than deposition. Other molecules investigated by qPCR did not show altered expression (Supporting Fig. 6b in File S1).

Absence of DPP3 augments bone loss in a murine model of estrogen deprivation–induced bone loss

To assess whether DPP3 might be relevant to common bone pathologies, we exploited the OVX-induced bone loss murine model, which stimulates bone resorption through estrogen withdrawal in mice, thus mimicking human postmenopausal osteoporosis.[60] First, we assessed whether DPP3 expression and activity were affected in this experimental condition. We performed bilateral OVX or SHAM operation in WT female mice. Six weeks later, we confirmed estrogen withdrawal by uterus weight reduction and consequent body weight gain (data not shown), and bone loss by tissue histology in OVX versus SHAM mice, as expected (Fig. 9A). Moreover, we observed reduced DPP3 expression by bone immunohistochemistry and significantly reduced DPP3 enzymatic activity in BM extracts of OVX mice as compared to the control group (Fig. 9A,B). Then, we repeated the surgery in WT and *Dpp3* KO female, in parallel. In addition, μCT analysis showed the expected changes in bone histomorphometric parameters: both in the WT and in *Dpp3* KO, the BV/TV ratio, Tb.Th and trabecular number (Tb.N) decreased in OVX mice as compared to SHAM. More importantly, the BV/TV ratio, Tb.Th, and Tb.N were significantly lower, while the BS/BV ratio and Tb.Sp were significantly higher in *Dpp3* KO mice as compared to WT after OVX. For all measured parameters, a slight alteration was found between *Dpp3* KO and WT mice in the SHAM group (Fig. 9C, Supporting Table 2 in File S1). Overall, these results showed that lack of DPP3 augmented bone loss after estrogen withdrawal in female mice, and confirmed the relevance of DPP3 in the framework of bone physiopathology.

Discussion

In the present work, we investigated the role of DPP3 in bone homeostasis through in vitro and in vivo studies, taking advantage of our newly generated *Dpp3* KO mouse model. We demonstrated that lack of DPP3 led to a bone loss phenotype mainly owing to increased OC resorptive activity. This was fostered by chronic exposure to increased oxidative stress because of increased ROS production and reduced antioxidant capacity specifically related to impaired activity of the Nrf2/HO-1 pathway, and to a low-grade inflammatory status. These alterations determined the establishment of a persistent pro-osteoclastogenic environment in the bone of *Dpp3* KO mice; in fact, μCT analysis in younger mice did not detect structural alterations in *Dpp3* KO versus WT bones, whereas a defect was evident in older animals. On the other hand, the pathological environment reduced bone formation.

The Keap1/Nrf2 cytoprotective pathway is ubiquitous, thus skeletal cell intrinsic and secondary defects likely contributed to the observed pathological condition. In fact, on one hand, in vitro studies confirmed increased *Dpp3* KO OC activity, reduced expression of Nrf2 and HO-1, and altered redox balance with increased and sustained ROS production by *Dpp3* KO OC precursors, ultimately resulting in augmented apoptosis; a similar behavior was observed in vitro in PMN cells. On the other hand, we observed an increased in vitro *Dpp3* KO OB activity at variance with the impairment found in vivo. This discrepancy was reconciled in co-culture experiments, which suggested an impaired OB/OC crosstalk in the absence of DPP3 and further highlighted the important role of the microenvironment in directing cell behavior.

Lack of appropriate antioxidant and cytoprotective function can aggravate coincident pathological conditions; accordingly, lack of DPP3 augmented the bone loss caused by estrogen deprivation in the OVX mouse model of human postmenopausal osteoporosis. Interestingly, we also found that DPP3 was reduced in WT OVX mice as compared to SHAM; this adds translational relevance to our results and paves the way to further investigating DPP3 in osteoporotic patients.

Here we also presented preliminary data suggesting a possible immune dysregulation in the *Dpp3* KO mouse, namely significantly increased ROS production by PMN and macrophages, and altered T cells subsets with expansion of memory T (data not shown). In fact, DPP3 is also expressed in cells of the innate and adaptive immunity,[42,61] and recent work proposed that DPP3, released by nonimmunogenic necrotic cells after loss of cellular integrity, might modulate adaptive immunity.[62] Therefore, based on the well-known interplay between bone and the immune system, our work could lay the foundation for the thorough dissection of DPP3 function in both compartments.

Our data show that the inactivation of different genes along the Nrf2 pathway leads to similar skeletal phenotypes, which underlines the importance of this signaling in bone metabolism. In fact, as far as we investigated, in many aspects *Dpp3* gene inactivation led to a phenotype closely resembling the condition displayed in *Nrf2* KO and in *Ho-1* KO mouse. [20,63,64] Moreover, because Nrf2 is known to take also part in other important cellular processes, such as proteostasis maintenance and endoplasmic reticulum stress quenching, [65,66] absence of DPP3 might also have a detrimental effect in those Nrf2-related contexts, which have not been addressed here.

Nrf2 pathway activation by DPP3 has been clearly shown to be independent of DPP3 enzymatic activity.[30] In this respect, we showed almost complete lack of enzymatic function in vitro in our *Dpp3* KO mouse using a standard synthetic substrate, but we did not systematically look for DPP3 substrate in vivo. A series of compounds have been proposed to play this role, mainly through in vitro studies.[24] Recently, DPP3 was reported to effectively digest the Angiotensin-II peptide and to exert a critical function in blood pressure control during hypertension,[25,26] possibly through Nrf2 regulation.[27] The association between hypertension and BMD is indeed debated[67]; therefore, based on literature and on our results it would be interesting to further investigate this aspect taking advantage of our newly generated *Dpp3* KO mouse.

In conclusion, we demonstrated a nonredundant role for DPP3 in the maintenance of bone homeostasis. Prompted by our results, we believe DPP3 could deserve attention also in human physiopathology to define whether it might represent a possible new osteoimmunological player and a marker of pathology.

Supplementary Material

Refer to Web version on PubMed Central for supplementary material.

Acknowledgments

References

1. Florencio-Silva R, Sasso GR, Sasso-Cerri E, Simoes MJ, Cerri PS. Biology of bone tissue: structure, function, and factors that influence bone cells. Biomed Res Int. 2015;2015:421746 [PubMed: 26247020]

2. Han Y, You X, Xing W, Zhang Z, Zou W. Paracrine and endocrine actions of bone—the functions of secretory proteins from osteoblasts, osteocytes, and osteoclasts. Bone Res. 2018;6:16. [PubMed: 29844945]

3. Kenkre JS, Bassett J. The bone remodelling cycle. Ann Clin Biochem. 2018;55(3):308–27. [PubMed: 29368538]

4. Medina-Gomez C, Kemp JP, Trajanoska K, et al. Life-course genome-wide association study meta-analysis of total body BMD and assessment of age-specific effects. Am J Hum Genet. 2018;102(1):88–102. [PubMed: 29304378]

5. Domazetovic V, Marcucci G, Iantomasi T, Brandi ML, Vincenzini MT. Oxidative stress in bone remodeling: role of antioxidants. Clin Cases Miner Bone Metab. 2017;14(2):209–16. [PubMed: 29263736]

6. Manolagas SC. From estrogen-centric to aging and oxidative stress: a revised perspective of the pathogenesis of osteoporosis. Endocr Rev. 2010;31(3):266–300. [PubMed: 20051526]

7. Thannickal VJ, Fanburg BL. Reactive oxygen species in cell signaling. Am J Physiol Lung Cell Mol Physiol. 2000;279(6):L1005–28. [PubMed: 11076791]

8. Gostner JM, Becker K, Fuchs D, Sucher R. Redox regulation of the immune response. Redox Rep. 2013;18(3):88–94. [PubMed: 23601165]

9. Bryan HK, Olayanju A, Goldring CE, Park BK. The Nrf2 cell defence pathway: Keap1-dependent and -independent mechanisms of regulation. Biochem Pharmacol. 2013;85(6):705–17. [PubMed: 23219527]

10. Zhang Q, Pi J, Woods CG, Andersen ME. A systems biology perspective on Nrf2-mediated antioxidant response. Toxicol Appl Pharmacol. 2010;244(1):84–97. [PubMed: 19716833]

11. Reichard JF, Motz GT, Puga A. Heme oxygenase-1 induction by NRF2 requires inactivation of the transcriptional repressor BACH1. Nucleic Acids Res. 2007;35(21):7074–86. [PubMed: 17942419]

12. Kanzaki H, Shinohara F, Itohiya K, et al. RANKL induces Bach1 nuclear import and attenuates Nrf2-mediated antioxidant enzymes, thereby augmenting intracellular reactive oxygen species signaling and osteoclastogenesis in mice. FASEB J. 2017;31(2):781–92. [PubMed: 27836987]

13. Yamazaki H, Tanji K, Wakabayashi K, Matsuura S, Itoh K. Role of the Keap1/Nrf2 pathway in neurodegenerative diseases. Pathol Int. 2015;65(5):210–9. [PubMed: 25707882]

14. Smallwood MJ, Nissim A, Knight AR, Whiteman M, Haigh R, Winyard PG. Oxidative stress in autoimmune rheumatic diseases. Free Radic Biol Med. 2018;125:3–14. [PubMed: 29859343]

15. Hishikawa A, Hayashi K, Itoh H. Transcription factors as therapeutic targets in chronic kidney disease. Molecules. 2018;23(5):1123 10.3390/molecules23051123.

16. Satta S, Mahmoud AM, Wilkinson FL, Alexander MY, White SJ. The role of Nrf2 in cardiovascular function and disease. Oxid Med Cell Longev. 2017;2017:9237263 10.1155/2017/9237263. [PubMed: 29104732]

17. Zhao H, Eguchi S, Alam A, Ma D. The role of nuclear factor-erythroid 2 related factor 2 (Nrf-2) in the protection against lung injury. Am J Physiol Lung Cell Mol Physiol. 2017;312(2):L155–62. [PubMed: 27864288]

18. O'Connell MA, Hayes JD. The Keap1/Nrf2 pathway in health and disease: from the bench to the clinic. Biochem Soc Trans. 2015;43(4): 687–9. [PubMed: 26551713]

19. Lippross S, Beckmann R, Streubesand N, et al. Nrf2 deficiency impairs fracture healing in mice. Calcif Tissue Int. 2014;95(4):349–61. [PubMed: 25096517]

20. Ibanez L, Ferrandiz ML, Brines R, Guede D, Cuadrado A, Alcaraz MJ. Effects of Nrf2 deficiency on bone microarchitecture in an experimental model of osteoporosis. Oxid Med Cell Longev. 2014;2014: 726590. [PubMed: 25120886]

21. Wruck CJ, Fragoulis A, Gurzynski A, et al. Role of oxidative stress in rheumatoid arthritis: insights from the Nrf2-knockout mice. Ann Rheum Dis. 2011;70(5):844–50. [PubMed: 21173018]

22. Marchev AS, Dimitrova PA, Burns AJ, Kostov RV, Dinkova-Kostova AT, Georgiev MI. Oxidative stress and chronic inflammation in osteoarthritis: can NRF2 counteract these partners in crime? Ann N Y Acad Sci. 2017;1401(1):114–35. [PubMed: 28662306]

23. Hast BE, Goldfarb D, Mulvaney KM, et al. Proteomic analysis of ubiquitin ligase KEAP1 reveals associated proteins that inhibit NRF2 ubiquitination. Cancer Res. 2013;73(7):2199–210. [PubMed: 23382044]

24. Prajapati SC, Chauhan SS. Dipeptidyl peptidase III: a multifaceted oligopeptide N-end cutter. FEBS J. 2011;278(18):3256–76. [PubMed: 21794094]

25. Pang X, Shimizu A, Kurita S, et al. Novel therapeutic role for dipeptidyl peptidase III in the treatment of hypertension. Hypertension. 2016;68 (3):630–41. [PubMed: 27456521]

26. Cruz-Diaz N, Wilson BA, Pirro NT, Brosnihan KB, Marshall AC, Chappell MC. Identification of dipeptidyl peptidase 3 as the Angiotensin-(1–7) degrading peptidase in human HK-2 renal epithelial cells. Peptides. 2016;83:29–37. [PubMed: 27315786]

27. Sato A, Ogita H. Pathophysiological implications of dipeptidyl peptidases. Curr Protein Pept Sci. 2017;18(8):843–9. [PubMed: 28356045]

28. Singh R, Sharma MC, Sarkar C, Singh M, Chauhan SS. Transcription factor C/EBP-beta mediates downregulation of dipeptidyl-peptidase III expression by interleukin-6 in human glioblastoma cells. FEBS J. 2014;281(6):1629–41. [PubMed: 24472318]

29. Prajapati SC, Chauhan SS. Human dipeptidyl peptidase III mRNA variant I and II are expressed concurrently in multiple tumor derived cell lines and translated at comparable efficiency in vitro. Mol Biol Rep. 2016;43(6):457–62. [PubMed: 27153830]

30. Lu K, Alcivar AL, Ma J, et al. NRF2 induction supporting breast cancer cell survival is enabled by oxidative stress-induced DPP3-KEAP1 interaction. Cancer Res. 2017;77(11):2881–92. [PubMed: 28416489]

31. Abramic M, Simaga S, Osmak M, et al. Highly reactive cysteine residues are part of the substrate binding site of mammalian dipeptidyl peptidases III. Int J Biochem Cell Biol. 2004;36(3):434–46. [PubMed: 14687922]

32. Dempster DW, Compston JE, Drezner MK, et al. Standardized nomenclature, symbols, and units for bone histomorphometry: a 2012 update of the report of the ASBMR Histomorphometry Nomenclature Committee. J Bone Miner Res. 2013;28(1):2–17. [PubMed: 23197339]

33. Bouxsein ML, Boyd SK, Christiansen BA, Guldberg RE, Jepsen KJ, Muller R. Guidelines for assessment of bone microstructure in rodents using micro-computed tomography. J Bone Miner Res. 2010;25(7):1468–86. [PubMed: 20533309]

34. Blair HC, Kalyvioti E, Papachristou NI, et al. Apolipoprotein A-1 regulates osteoblast and lipoblast precursor cells in mice. Lab Invest. 2016;96(7):763–72. [PubMed: 27088511]

35. Liu L, Alonso V, Guo L, et al. Na+/H+ exchanger regulatory factor 1 (NHERF1) directly regulates osteogenesis. J Biol Chem. 2012;287 (52):43312–21. [PubMed: 23109343]

36. Jacome-Galarza CE, Lee SK, Lorenzo JA, Aguila HL. Identification, characterization, and isolation of a common progenitor for osteoclasts, macrophages, and dendritic cells from murine bone marrow and periphery. J Bone Miner Res. 2013;28(5):1203–13. [PubMed: 23165930]

37. Menale C, Campodoni E, Palagano E, et al. Mesenchymal stromal cell-seeded biomimetic scaffolds as a factory of soluble RANKL in Rankl-deficient osteopetrosis. Stem Cells Transl Med. 2019;8(1): 22–34. [PubMed: 30184340]

38. Li Y, Toraldo G, Li A, et al. B cells and T cells are critical for the preservation of bone homeostasis and attainment of peak bone mass in vivo. Blood. 2007;109(9):3839–48. [PubMed: 17202317]

39. Marrella V, Lo Iacono N, Fontana E, et al. IL-10 critically modulates B cell responsiveness in Rankl–/– mice. J Immunol. 2015;194(9): 4144–53. [PubMed: 25825446]

40. Majima HJ, Nakanishi-Ueda T, Ozawa T. 4-Hydroxy-2-nonenal (4-HNE) staining by anti-HNE antibody. Methods Mol Biol. 2002;196:31–4. [PubMed: 12152210]

41. Mayadas TN, Cullere X, Lowell CA. The multifaceted functions of neutrophils. Annu Rev Pathol. 2014;9:181–218. [PubMed: 24050624]

42. Hashimoto J, Yamamoto Y, Kurosawa H, Nishimura K, Hazato T. Identification of dipeptidyl peptidase III in human neutrophils. Biochem Biophys Res Commun. 2000;273(2):393–7. [PubMed: 10873616]

43. Hemshekhar M, Thushara RM, Kumar SKN, et al. Bone degeneration, inflammation and secondary complications of arthritis: potential targets and their natural inhibitors. Mini Rev Med Chem. 2018;18(3): 244–75. [PubMed: 28302039]

44. Kanzaki H, Shinohara F, Kajiya M, Kodama T. The Keap1/Nrf2 protein axis plays a role in osteoclast differentiation by regulating intracellular reactive oxygen species signaling. J Biol Chem. 2013;288(32): 23009–20. [PubMed: 23801334]

45. Hyeon S, Lee H, Yang Y, Jeong W. Nrf2 deficiency induces oxidative stress and promotes RANKL-induced osteoclast differentiation. Free Radic Biol Med. 2013;65:789–99. [PubMed: 23954472]

46. Kanzaki H, Shinohara F, Kajiya M, Fukaya S, Miyamoto Y, Nakamura Y. Nuclear Nrf2 induction by protein transduction attenuates osteoclastogenesis. Free Radic Biol Med. 2014;77:239–48. [PubMed: 25224039]

47. Glorie L, D'Haese PC, Verhulst A. Boning up on DPP4, DPP4 substrates, and DPP4-adipokine interactions: logical reasoning and known facts about bone related effects of DPP4 inhibitors. Bone. 2016;92:37–49. [PubMed: 27535784]

48. Kim H, Baek KH, Lee SY, et al. Association of circulating dipeptidyl-peptidase 4 levels with osteoporotic fracture in postmenopausal women. Osteoporos Int. 2017;28(3):1099–108. [PubMed: 27866216]

49. Ha H, Kwak HB, Lee SW, et al. Reactive oxygen species mediate RANK signaling in osteoclasts. Exp Cell Res. 2004;301(2):119–27. [PubMed: 15530848]

50. Yamaguchi Y, Kanzaki H, Katsumata Y, et al. Dimethyl fumarate inhibits osteoclasts via attenuation of reactive oxygen species signalling by augmented antioxidation. J Cell Mol Med. 2018;22(2):1138–47. [PubMed: 29063666]

51. Zani IA, Stephen SL, Mughal NA, et al. Scavenger receptor structure and function in health and disease. Cell. 2015;4(2):178–201.

52. Zhou JH, Broussard SR, Strle K, et al. IL-10 inhibits apoptosis of promyeloid cells by activating insulin receptor substrate-2 and phosphatidylinositol 3′-kinase. J Immunol. 2001;167(8):4436–42. [PubMed: 11591769]

53. Michalski MN, Koh AJ, Weidner S, Roca H, McCauley LK. Modulation of osteoblastic cell efferocytosis by bone marrow macrophages. J Cell Biochem. 2016;117(12):2697–706. [PubMed: 27061191]

54. Rached MT, Kode A, Xu L, et al. FoxO1 is a positive regulator of bone formation by favoring protein synthesis and resistance to oxidative stress in osteoblasts. Cell Metab. 2010;11(2):147–60. [PubMed: 20142102]

55. Barbagallo I, Vanella A, Peterson SJ, et al. Overexpression of heme oxygenase-1 increases human osteoblast stem cell differentiation. J Bone Miner Metab. 2010;28(3):276–88. [PubMed: 19924377]

56. Morikawa D, Nojiri H, Saita Y, et al. Cytoplasmic reactive oxygen species and SOD1 regulate bone mass during mechanical unloading. J Bone Miner Res. 2013;28(11):2368–80. [PubMed: 23674366]

57. Maeda K, Kobayashi Y, Udagawa N, et al. Wnt5a-Ror2 signaling between osteoblast-lineage cells and osteoclast precursors enhances osteoclastogenesis. Nat Med. 2012;18(3):405–12. [PubMed: 22344299]

58. Pederson L, Ruan M, Westendorf JJ, Khosla S, Oursler MJ. Regulation of bone formation by osteoclasts involves Wnt/BMP signaling and the chemokine sphingosine-1-phosphate. Proc Natl Acad Sci U S A. 2008;105(52):20764–9. [PubMed: 19075223]

59. Zhao C, Irie N, Takada Y, et al. Bidirectional ephrinB2-EphB4 signaling controls bone homeostasis. Cell Metab. 2006;4(2):111–21. [PubMed: 16890539]

60. Li JY, Adams J, Calvi LM, Lane TF, Weitzmann MN, Pacifici R. Ovariectomy expands murine short-term hemopoietic stem cell function through T cell expressed CD40L and Wnt10B. Blood. 2013;122(14):2346–57. [PubMed: 23954891]

61. Grdisa M, Vitale L. Types and localization of aminopeptidases in different human blood cells. Int J Biochem. 1991;23(3):339–45. [PubMed: 2044841]

62. Gamrekelashvili J, Kapanadze T, Han M, et al. Peptidases released by necrotic cells control CD8+ T cell cross-priming. J Clin Invest. 2013; 123(11):4755–68. [PubMed: 24216478]

63. Sun YX, Li L, Corry KA, et al. Deletion of Nrf2 reduces skeletal mechanical properties and decreases load-driven bone formation. Bone. 2015;74:1–9. [PubMed: 25576674]

64. Florczyk-Soluch U, Jozefczuk E, Stepniewski J, et al. Various roles of heme oxygenase-1 in response of bone marrow macrophages to RANKL and in the early stage of osteoclastogenesis. Sci Rep. 2018;8 (1):10797. [PubMed: 30018287]

65. Pajares M, Cuadrado A, Rojo AI. Modulation of proteostasis by transcription factor NRF2 and impact in neurodegenerative diseases. Redox Biol. 2017;11:543–53. [PubMed: 28104575]

66. Mukaigasa K, Tsujita T, Nguyen VT, et al. Nrf2 activation attenuates genetic endoplasmic reticulum stress induced by a mutation in the phosphomannomutase 2 gene in zebrafish. Proc Natl Acad Sci U S A. 2018;115(11):2758–63. [PubMed: 29472449]

67. Ye Z, Lu H, Liu P. Association between essential hypertension and bone mineral density: a systematic review and meta-analysis. Oncotarget. 2017;8(40):68916–27. [PubMed: 28978167]
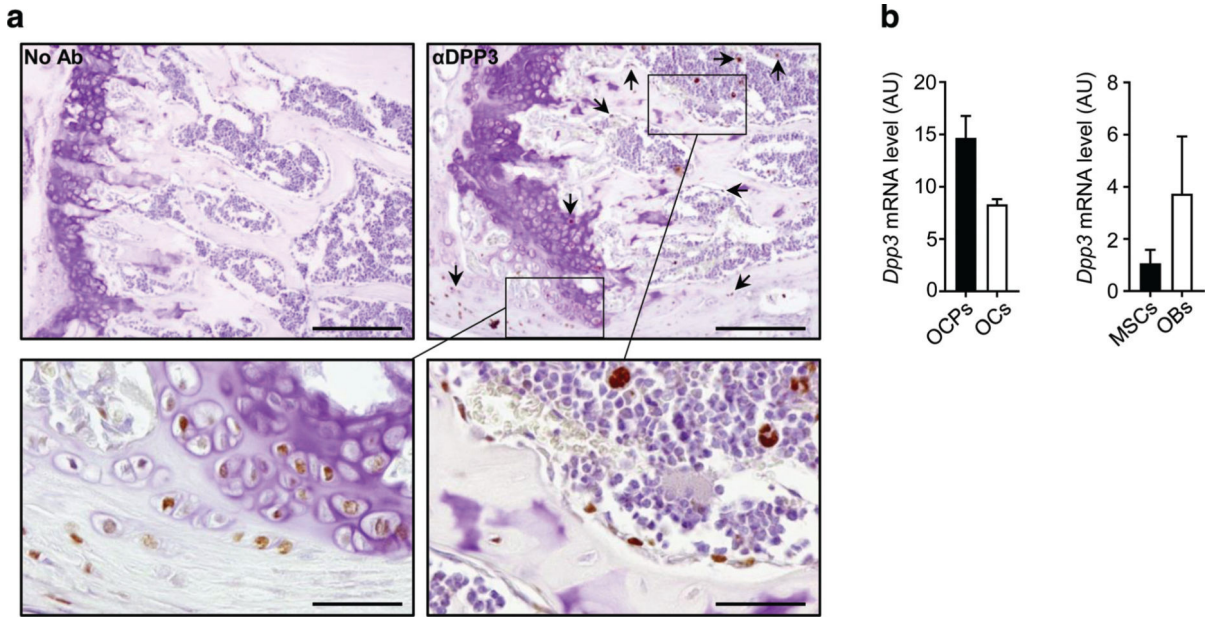
Author Manuscript

Author Manuscript

Author Manuscript

Author Manuscript

Fig. 1.
DPP3 is expressed in the bone tissue. (*A*) Representative images of immunohistochemical analysis of DPP3 expression in the femur of WT C57BL/6J mouse. Upper left, negative control; upper right and lower left and right, staining with mouse antibody αDPP3 at different magnification. Scale bars = upper panels 200 μm; lower panels 50 μm. Arrows indicate representative positive cells. (*B*) qPCR for murine *Dpp3* expression in in vitro osteoclastogenesis (*n* = 3) and osteoblastogenesis (*n* = 2). In the latter, bars indicate the range. For each evaluation, *n* 2. DPP3 = dipeptidyl peptidase 3; OCP = osteoclast precursor; OC = osteoclast; MSC = mesenchymal stromal cell; OB = osteoblast.
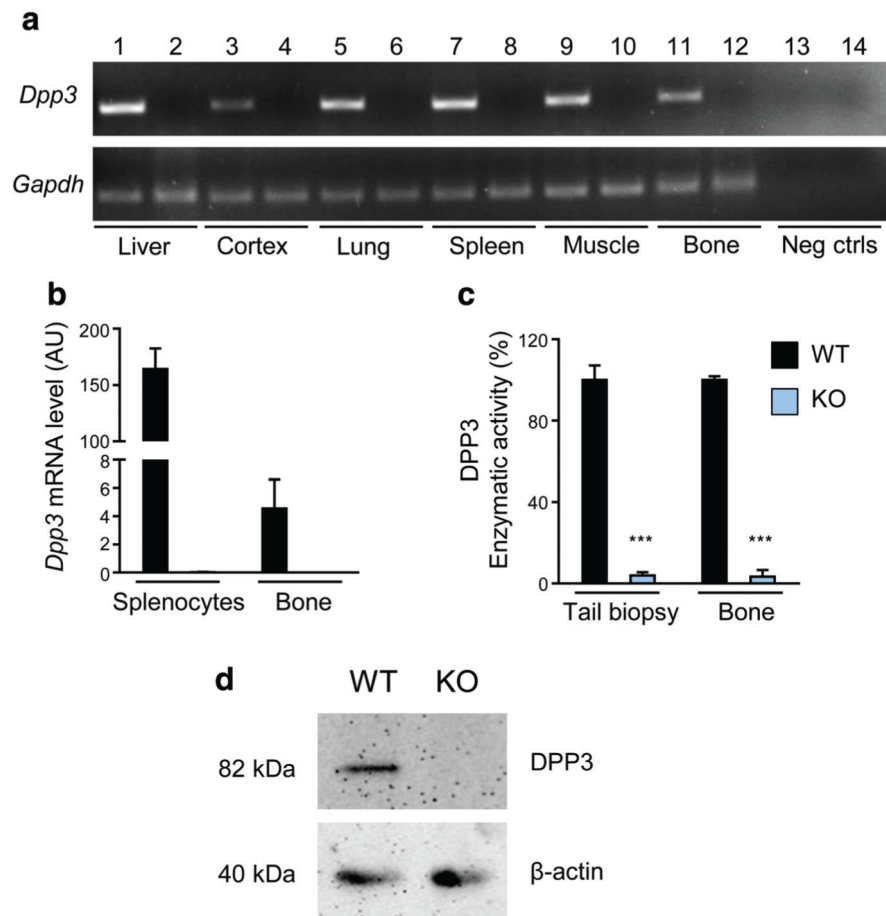
Fig. 2.
Dpp3 gene expression and enzymatic activity are effectively shut down in the *Dpp3* KO mouse model. (*A*) Representative RT-PCR for *Dpp3* gene expression in several tissues obtained from WT (odd numbers) and *Dpp3* KO (even numbers) mice. (*B*) qPCR of *Dpp3* gene on splenocytes and total bone from WT and *Dpp3* KO mice ($n = 3$ per genotype). (*C*) Evaluation of DPP3 enzymatic activity in WT. (*E*) *Dpp3* KO mice in protein extracts from tail biopsies and total bone (n 3 per genotype). The Arg-Arg-2-naphthylamide peptide was used as reaction substrate. The enzymatic activity was quantified by spectrophotometric analysis. Data are presented as the mean ± SE. ***$p < .001$. (*D*) Representative Western blot analysis of *Dpp3* protein in total bone tissue from WT and *Dpp3* KO mice. β-actin = loading control; *Gapdh* = housekeeping control.
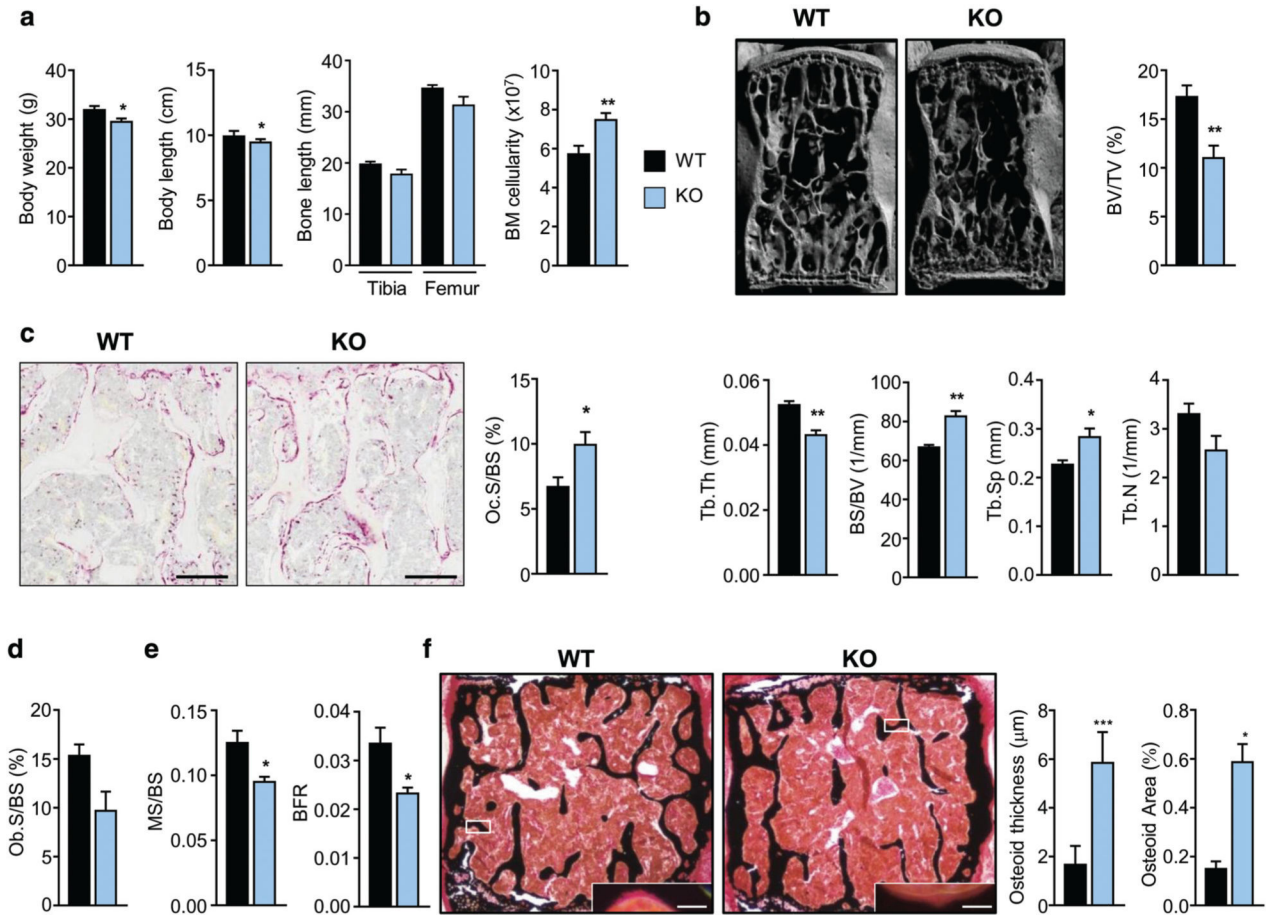
Fig. 3.
The *Dpp3* KO mouse model displays a bone loss phenotype. (*A*) Body weight, body length, long-bone length, and BM cellularity from one femur and one tibia per mouse, in WT and *Dpp3* KO mice. (*B*) μCT analysis of lumbar vertebrae: 3D reconstruction and static histomorphometric analysis of trabecular bone in WT and *Dpp3* KO mice. (*C*) Representative images of decalcified paraffin-embedded TRAP-stained sections of WT and *Dpp3* KO bone, and quantification of Oc.S/BS. Scale bar = 200 μm. (*D*) Ob.S/BS ratio, as assessed through ALP-staining of WT and *Dpp3* KO lumbar vertebrae. (*E*) Dynamic histomorphometric analysis. (*F*) Representative images of mineralized resin-embedded von Kossa-stained vertebrae of WT and *Dpp3* KO mice, and corresponding quantization of osteoid thickness and area. Scale bar = 150 μm and 5 μm, for the lower magnification and the inset, respectively. All the evaluations were performed in 6-month-old male mice. For each evaluation, $n \geq 6$ per genotype. *$p < .05$, **$p < .01$, ***$p < .001$. BM = bone marrow; 3D = three-dimensional; Oc.S/BS = osteoclast surface/bone surface; Ob.S/BS = osteoblast surface/bone surface.
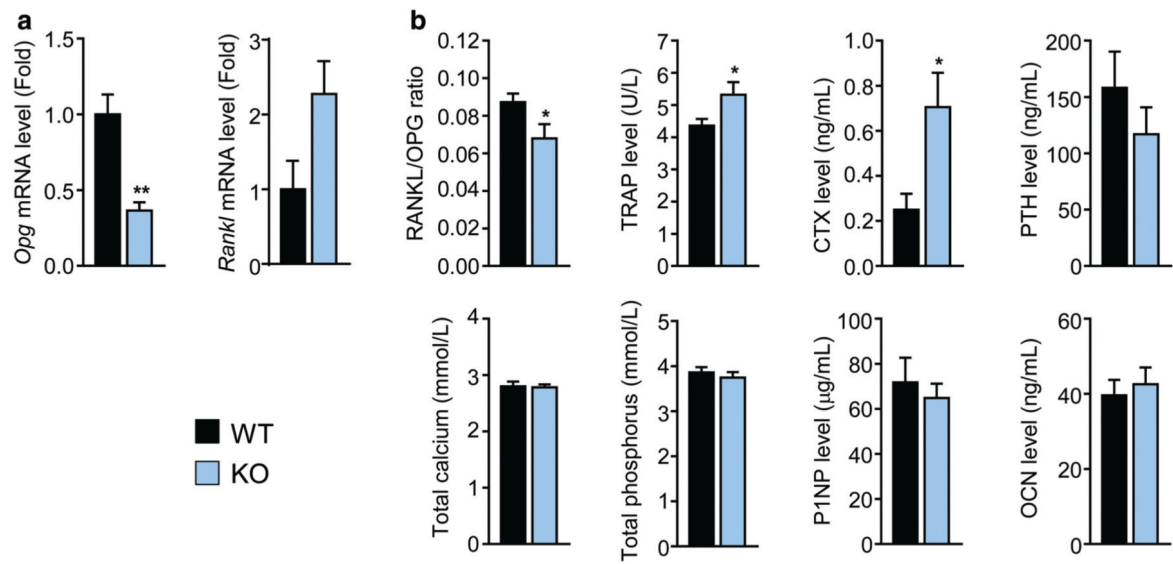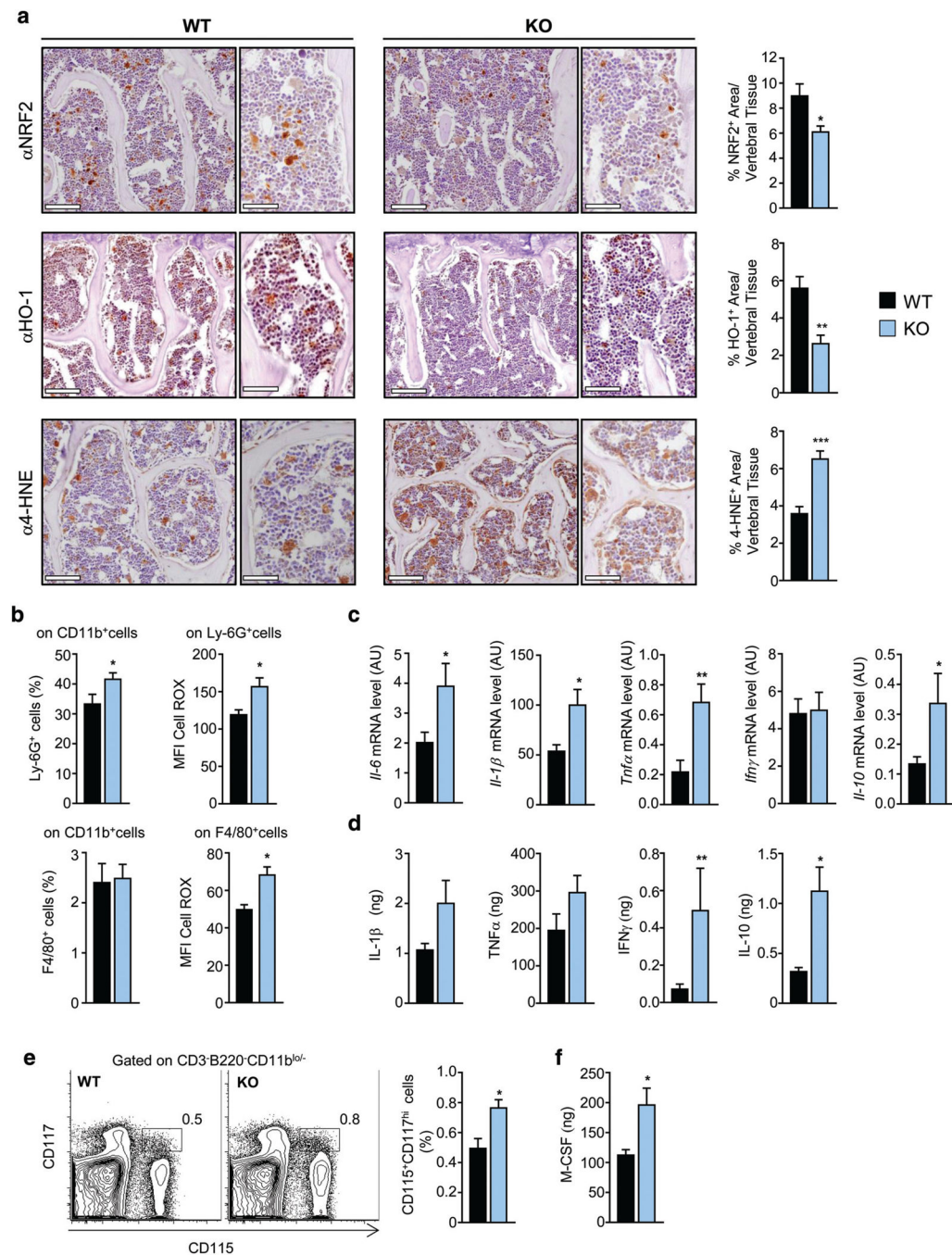
Fig. 4.
Lack of DPP3 alters bone metabolism. (*A*) qPCR of Opg and Rankl gene expression in total bone from WT and *Dpp3* KO mice. (*B*) Serological analysis of markers of bone metabolism. For each evaluation, n 6 per genotype. $*p < .05$, $**p < .01$.

Fig. 5.
Absence of DPP3 leads to increased oxidative stress and inflammation in the bone tissue.
(*A*) Representative images, and corresponding high magnification, of sections of decalcified paraffin-embedded vertebrae of WT and *Dpp3* KO stained with antibodies against Nrf2, HO-1, and 4-HNE, and corresponding quantization. Scale bar = 100 μm for lower magnification, and 50 μm for higher magnification images. (*B*) Upper panels: frequency of PMNs (as percentage of Ly-6G$^+$ after gating on CD11b$^+$ cells) and corresponding amount of ROS production as MFI in the BM of WT and *Dpp3* KO mice. Lower panels: frequency of

macrophages (as percentage of F4/80$^+$ after gating on CD11b$^+$ cells) and corresponding amount of ROS production as MFI, in the BM of WT and *Dpp3* KO mice. (*C*) qPCR of genes coding for inflammatory cytokines in the BM cells of WT and *Dpp3* KO mice. (*D*)Quantification of amount of inflammatory cytokines in the BM supernatant of WT and *Dpp3* KO mice. (*E*) Representative plot of FACS analysis of CD115$^+$CD117^{hi} cells in WT and *Dpp3* KO BM, and corresponding quantification. (*F*) Quantification of M-CSF amount in the BM supernatant of WT and *Dpp3* KO mice. For each evaluation, *n* 6 per genotype. *$p < .05$, **$p < .01$. PMN = polymorphonuclear cell; MFI = meanfluorescence intensity.
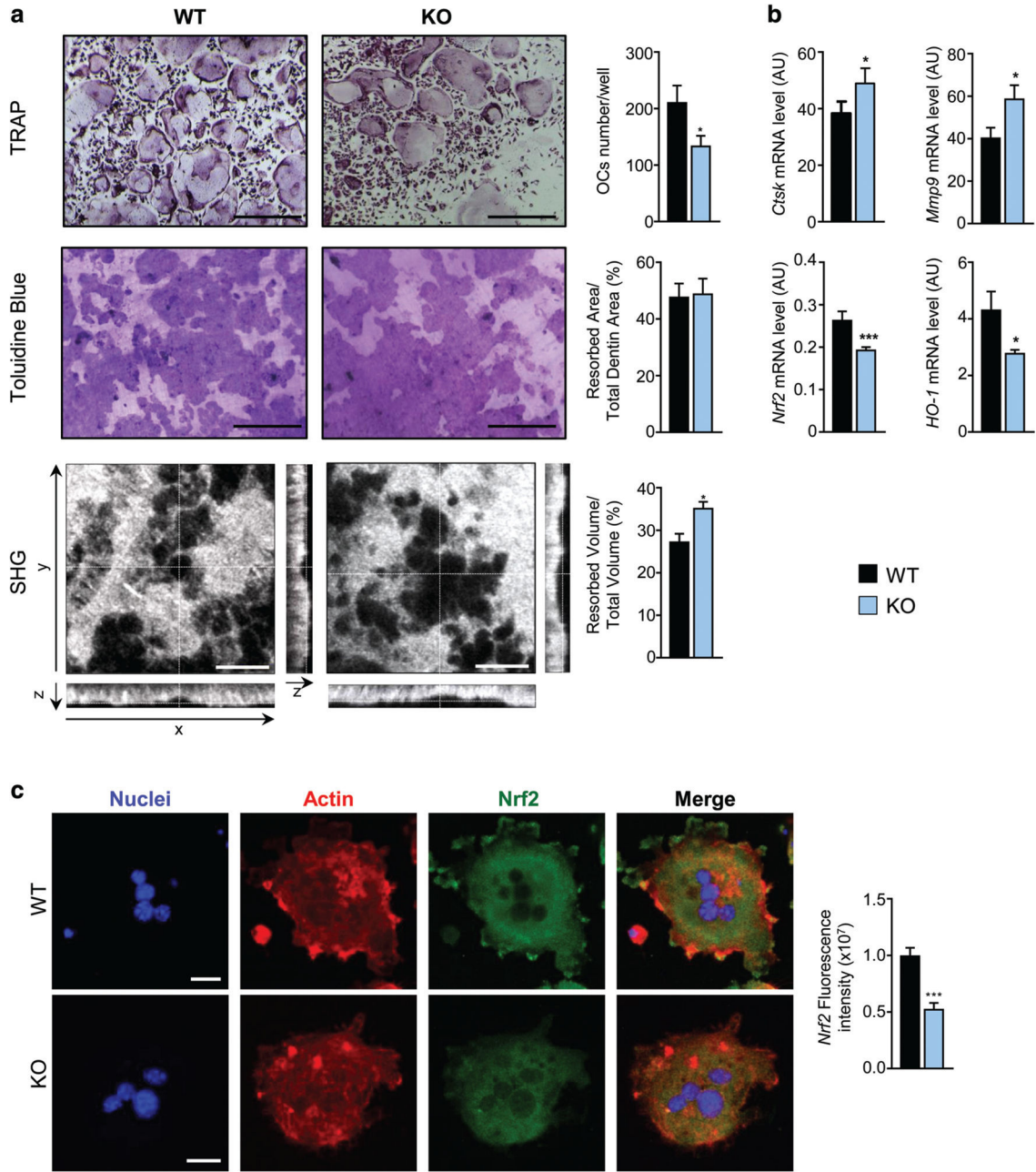
Fig. 6.
Loss of DPP3 increases in vitro osteoclast resorption activity and impairs Nrf2 signaling. (*A*) Upper panels: representative images of TRAP-stained in vitro differentiated osteoclasts from WT and *Dpp3* KO osteoclast precursors. Middle panels: Toluidine blue–stained resorption pits on dentin. Scale bar = 400 μm. Lower panels: SHG of dentin collagen in the different projections. Scale bar = 40 μm. Graphs on the right represent quantification analysis for each evaluation. (*B*) qPCR analysis of osteoclast functional genes and Nrf2 pathway in in vitro–differentiated WT and *Dpp3* KO osteoclasts. For each evaluation, *n* 6 per genotype. (*C*) Representative images of immunofluorescence analysis of in vitro–

differentiated WT and *Dpp3* KO osteoclasts stained as indicated, and Nrf2 fluorescence intensity. $*p < .05$, $***p < .001$. SHG = second harmonic generation.
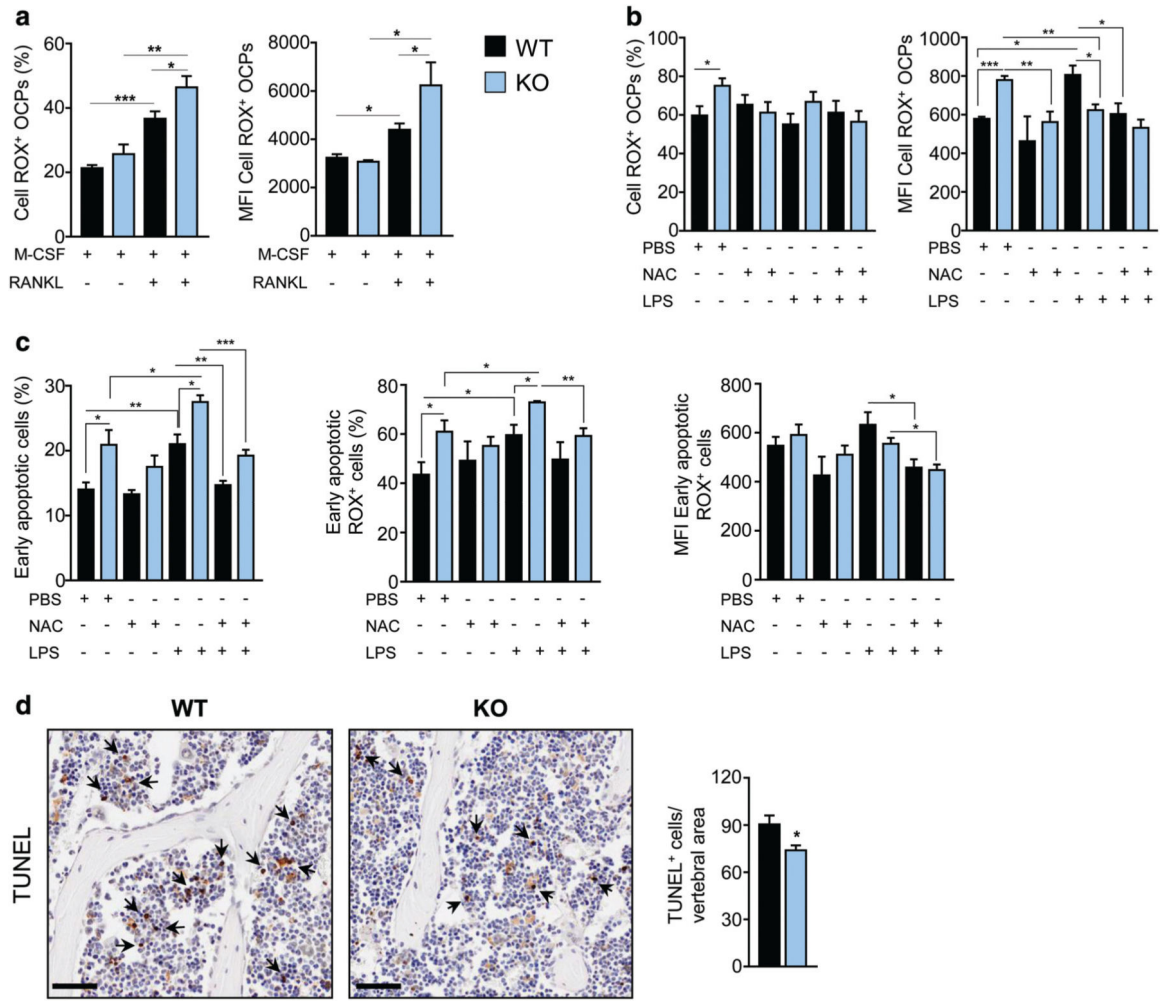
Fig. 7.

Dpp3 KO osteoclast precursor cells display higher ROS production and proneness to apoptosis. (*A*, *B*) Percentage of ROS+ WT and *Dpp3* KO OCPs and amount of ROS production expressed as MFI of ROS+ OCPs, as assessed by FACS analysis in the presence of the indicated stimuli. (*C*) Percentage of WT and *Dpp3* KO early apoptotic cells and measurements of ROS production in this cell population, assessed as in *A* and *B*. (D) Representative images of PFA-fixed paraffin-embedded bone of WT and *Dpp3* KO mice stained with TUNEL, and corresponding quantification. Scale bar = 50 μm. Arrows indicate representative positive cells. For each evaluation, *n* 4 per genotype per group. *$p <$ .05, **$p <$ .01, ***$p <$ .001. OPC = osteoclast precursor cell; MFI = mean fluorescence intensity.
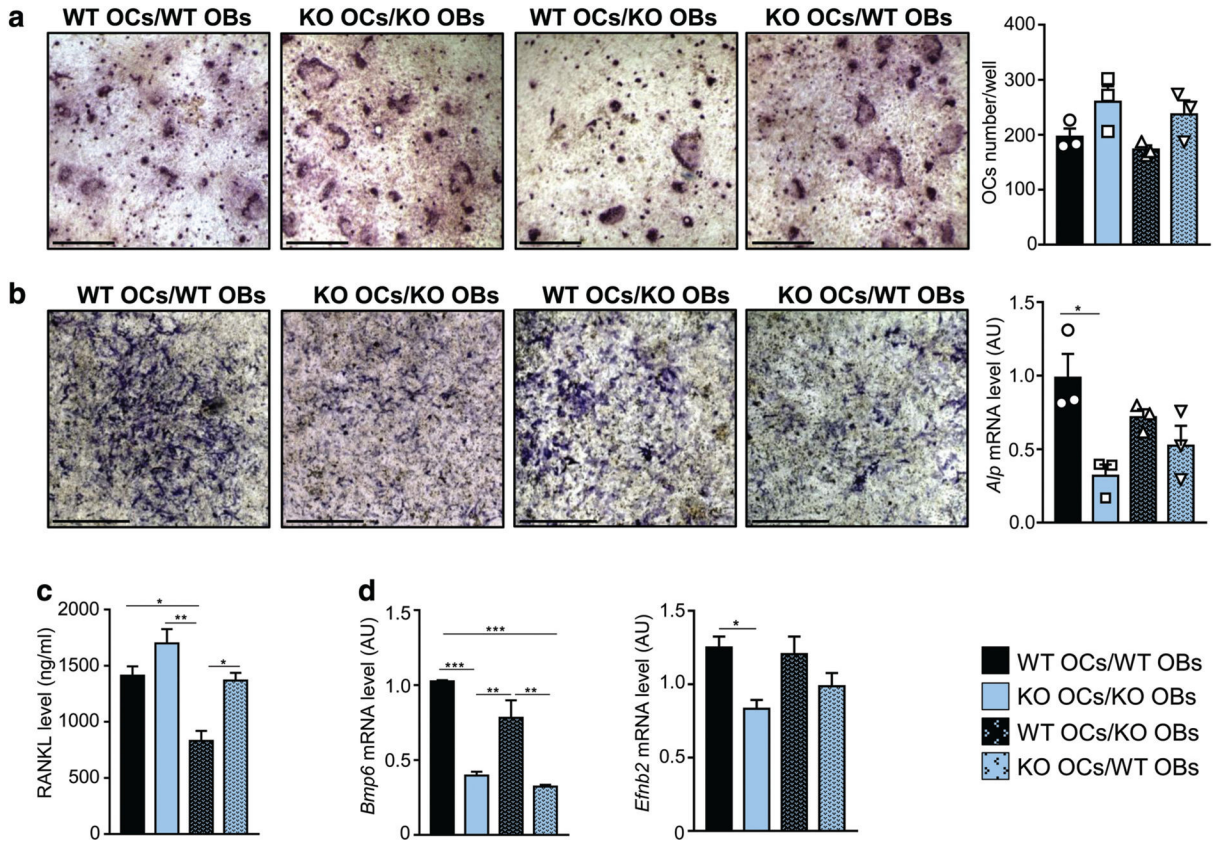
Fig. 8.

Lack of DPP3 causes altered osteoblast/osteoclast crosstalk. (*A*) Representative images of TRAP staining after osteoclast differentiation on dentin in the indicated co-culture conditions (scale bar = 400 μm), and corresponding osteoclast count. (*B*) Representative images of ALP staining in the indicated co-culture conditions (scale bar = 1 mm), and corresponding levels of *Alp* mRNA expression. (*C*) Quantization of RANKL cytokine in the co-culture supernatants. (*D*) Expression analysis of *Bmp6* and *Efnb2* as relevant genes for osteoclast/osteoblast crosstalk. For each experimental condition, $n = 3$. *$p < .05$, **$p < .01$, ***$p < .001$.
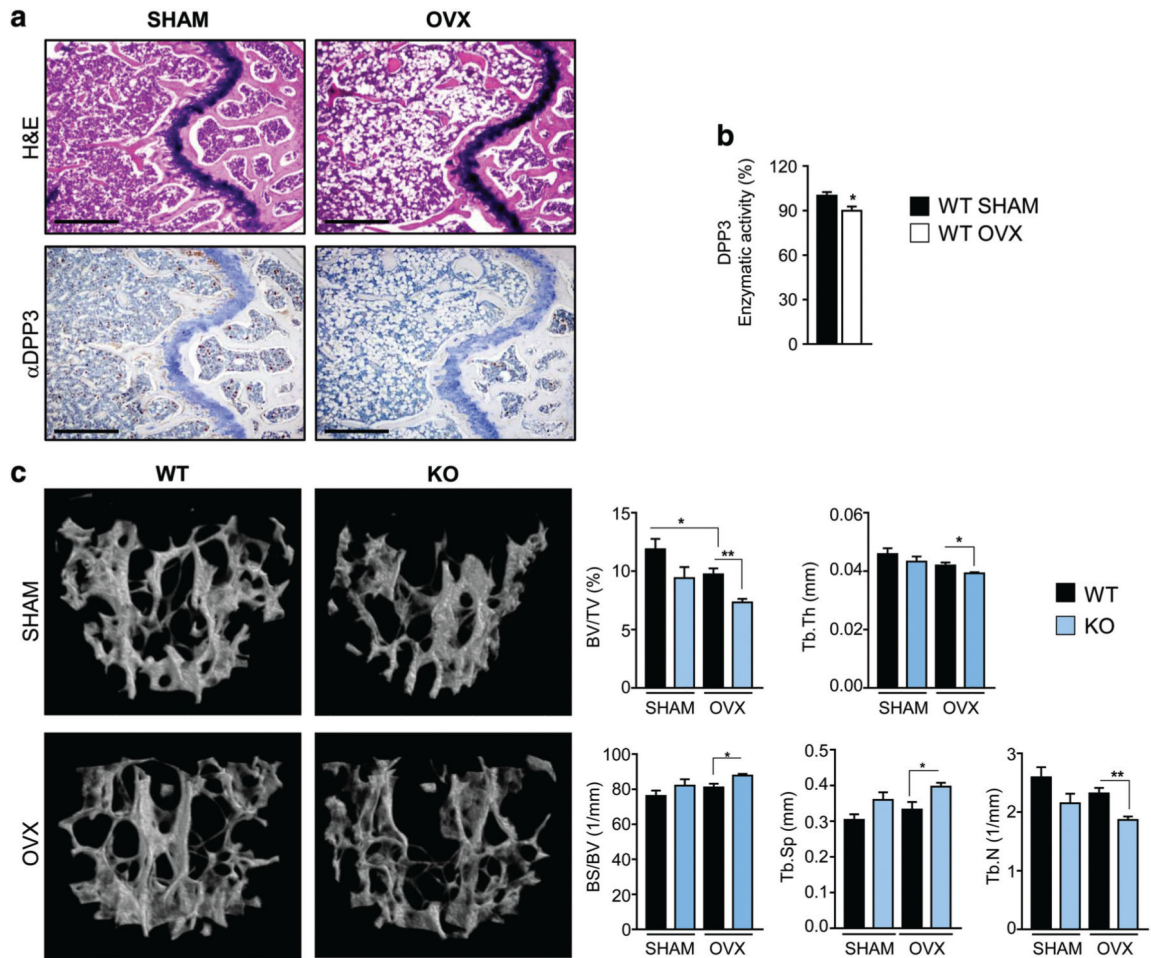
Fig. 9.
DPP3 activity correlates with estrogen status and lack of DPP3 augments bone loss after estrogen withdrawal. (*A*) Representative images of sections of decalcified paraffin-embedded femurs of SHAM and OVX WT mice stained with H&E (upper panels) and with anti-DPP3 antibody. Scale bar = 500 μm. (*B*) Evaluation of DPP3 enzymatic activity in SHAM and OVX WT mice in BM protein extracts; n 5 per group. (*C*) μCT analysis of the spine: 3D reconstruction and static histomorphometric analysis in SHAM and OVX WT and *Dpp3* KO mice. For each evaluation, n 5 per genotype per group. Only statistically significant comparisons are depicted; mean values ± SD for all the parameters measured, as well as detailed statistical analysis are reported in Supporting Table 2. *$p < .05$, **$p < .01$.